

Article

Dynamically Balanced Pointing System for CubeSats: Study and 3D Printing Manufacturing

Nicholas Sesto Gorella ^{*}, Matteo Caruso , Paolo Gallina  and Stefano Seriani 

Department of Engineering and Architecture, University of Trieste, Via A. Valerio 6/1, 34100 Trieste, Italy; matteo.caruso@phd.units.it (M.C.); pgallina@units.it (P.G.); sseriani@units.it (S.S.)

* Correspondence: nicholas.sestogorella@dia.units.it

Abstract: The increasing presence of additive manufacturing (AM) in the space sector prompted us to investigate the feasibility of a single *degree of freedom* (DoF) *pointing system* (PS) made by means of a *compound planetary gear train system* (C-PGTS) integrating a *dynamic balancing system* (DBS) and entirely realized in AM. We analyzed in detail the dynamics of the system dealing with the design and the realization of the prototype. Of fundamental importance for this paper is the careful selection of materials for AM suitable for the prohibitive conditions of space. The results, deriving from the comparison between the experimental part and the simulations, underline the correct dimensioning of the PS and the fundamental importance of DBS in maintaining the satellite attitude. The results also confirm the capabilities of AM in the production of complex mechanical systems, allowing high precision, combined with interesting mechanical properties and low weight. This suggests the potential of AM in the space domain, both for structural parts and active components, such as those listed in this work.

Keywords: CubeSat; 3D printing; pointing; dynamic balancing



Citation: Sesto Gorella, N.; Caruso, M.; Gallina, P.; Seriani, S. Dynamically Balanced Pointing System for CubeSats: Study and 3D Printing Manufacturing. *Robotics* **2021**, *10*, 121. <https://doi.org/10.3390/robotics10040121>

Academic Editor: Gursel Alici

Received: 24 August 2021
Accepted: 5 November 2021
Published: 8 November 2021

Publisher's Note: MDPI stays neutral with regard to jurisdictional claims in published maps and institutional affiliations.



Copyright: © 2021 by the authors. Licensee MDPI, Basel, Switzerland. This article is an open access article distributed under the terms and conditions of the Creative Commons Attribution (CC BY) license (<https://creativecommons.org/licenses/by/4.0/>).

1. Introduction

Since the late 1950s, the creation of artificial satellites has allowed mankind to both take a deeper look at the depths of outer space and to better understand how planet Earth behaves [1]. Nowadays, the constellation of devices in orbit around Earth provides a constant flow of data, allowing us to predict with sufficient accuracy the evolution of meteorological phenomena or to monitor the continuous changes occurring on the planet surface, i.e., cities development or the melting of the Arctic gravel [2,3]. Perhaps one of the most useful technological aspects to contemporary society is the introduction of the *global positioning system* (GPS). However, common satellites have high construction costs [4], making them hard to implement in most cases. Thanks to the progressive miniaturization of electronic components, toward the end of the 1990s, a miniaturized and standardized version of satellites, called CubeSat, based on cubic satellite units (1U) defined by the CubeSat design specification (CDS) with 100 mm long sides and with a maximum weight of 1.33 kg, was proposed [5]. Units can be combined into increasingly complex systems depending on the instruments they are equipped with. This new approach has made it possible for universities, and private entities with limited funds, to be able to put their equipment into orbit for an average cost, including manufacturing, of approximately EUR 60,000 per unit.

Furthermore, additive manufacturing technology is now a well-established process in today's technology landscape and is also becoming increasingly present in the aerospace sector [6], which is especially demanding in terms of construction quality and reliability. The first 3D-printed components to be implemented on an interplanetary space mission were the PBF-printed titanium wave guide supporting brackets on the Juno spacecraft, later followed by 3D-printed thrusters for the *attitude control system* (ACS) of the MEMPSI, Bevo-2, INSPIRE [7] and BioSentinel missions [8], fabricated with both *powder bed fusion* (PBF) and

selective laser sintering (SLA) techniques. Despite the rising presence of polymeric printed parts in CubeSat missions, as stated for satellite structures [9] and propulsion system [10], no evidence of a *fully* polymeric satellite has been found yet. The continuous improvement of 3D printer quality and printing algorithm efficiency is pushing the boundaries of additive manufacturing; however, the main problem is represented by the ability of the material to withstand the mechanical stresses generated by vibrations during the launch phase and by the considerable thermal excursions typical of LEO orbits [11,12]. A material that does not conform to space applications used, for example, for the construction of the CubeSat structure would lead to excessive deformations, affecting the alignment of optical or communication systems [13]. In addition, the high vacuum condition typical of a LEO orbit [14] threatens the satellite lifespan, due to the progressive loosening of polymeric material characteristics [15], caused by the evaporation of the material itself, the so-called *outgassing* phenomenon [16], and by the deposition of the material molecules on electric boards or optical instruments [17]. Despite the problems listed above related to materials, the advantages of 3D printing for space applications are of great importance. The possibility to print satellites directly in space, e.g., on the ISS, could greatly lower the cost of launch into orbit. Moreover, CubeSat missions have an estimated operational life ranging from days up to a few months, while the calculated success rate is about 60% [18], creating a necessity to remove the orbital debris composed by all the decommissioned satellites; a completely polymeric CubeSat would completely melt and disperse when re-entering into Earth's atmosphere [19].

Modern larger satellites are always equipped with an *attitude control system* (ACS) to maneuver and keep a desired attitude in space; on the other hand, CubeSats cannot always afford the added mass, cost and complexity. Three categories exist for ACSs: cold gas thrusters (CGT), which were developed for beyond the LEO mission, e.g., the MarCo CubeSat mission to Mars [7]; *magnetic TorQuers* (MTQs), which operate by means of magnets interacting with Earth's magnetic field; and mechanical ACS, which operate by means of *reaction wheels* (RWs). The combination of MTQs and RWs represents the most common solution for small satellites [20].

In most high-performance applications, where high-data throughput is requested along with attitude control toward specific targets (e.g., Earth or deep-space observation, or directional communications) the need arises to be able to point the satellite systems simultaneously toward two or more directions [21]. For example, in a real-time Earth observation scenario, the satellite is required to point its camera toward a specific point on the surface, while at the same time pointing its antenna toward the ground station or to another satellite. In larger satellites, this is generally achieved using an alt-azimuth mount on the antenna [22]; however this requires 2 degrees of freedom (DoF) and may prove impractical for small satellites.

In this work, we design and realize a single DoF *pointing system* (PS) capable of rotating a load composed by aligned CubeSat modules, while maintaining the attitude of the other unchanged with negligible input from the ACS. However, in coordination with the ACS, this system can be used to perform 2-DoF pointing as Figure 1a shows in relation to the orbital path. We achieve this by means of an integrated *dynamic balancing system* (DBS) based on a *counter-rotating flywheel* (CFW).

In Figure 1a, a diagram of the satellite is presented. It is composed of a fixed side containing the PS and DBS, aligned to the orbital path, and a rotating side (payload), which is kept pointed to a fixed point on Earth. Figure 1b describes the typical CubeSat configuration, where PS and DBS are needed. The fixed side, where the PS-DBS is installed in central position, keeps the communication with other satellites through an antenna (ADE), while the rotating load keeps a specific instrument, i.e., a lens telescope, pointed to a fixed point on Earth's surface. The first DoF acts on the z axis and, by means of the ACS, it is possible to add an extra DoF, providing a rotation around the y axis. Compared to MTQs and FWs, this system can be made very fast and, compared to CGT, more efficient. The counter rotation of the flywheel, with respect to the rotating side of the satellite,

is achieved by means of a reduction system. The spur gear and planetary gear drives represent roughly 58% of the total mechanical drives [23], thus promoting the study of solutions created through additive manufacturing [23,24], principally analyzing the effect of the printing parameters on the gear mechanical properties [25]. Once the 3D printing theory for spur gears is managed, a different reduction system can be obtained by simply changing positioning and coupling of the gear elements, ranging from the simple spur gear reduction system to the more complex and performing compound planetary gear transmission (C-PGT) [26,27]. Both the dynamic behavior of a satellite and that of a counter-rotating shaft can be modeled using the Lagrangian or Newtonian formulation, as the wide corpus of literature on planetary gears reduction systems shows [28–31]. It is thus possible to compare the analytic solution with the full-scale prototype experiment. This system is driven by a simple electronic control, based on a CubeSat satellite flywheel energy storage system (FESS) [32]. The work presented in this paper aims to contribute to the state of the art concerning 3D-printed mechanical systems for space applications. While in the state of the art, there are already 3D-printed structural elements for space applications, there is no evidence of such a dynamic system as that presented in the paper. The paper is organized as follows. In Section 2.1, starting from the operating conditions of the satellite and the engineering requirements, the reader finds the kinematic and dynamic study of the pointing system. The same section introduces selection criteria for the printable materials and presents an overview of the actuation system.

Section 3 presents the set-up of the multi-body simulation, the design of the prototype, followed by the experimental setup. In Section 4, the results are presented and discussed. Finally, in Section 5, the successes and drawbacks of the design are highlighted in order to further contribute to the state of the art and to build the foundation for future developments.

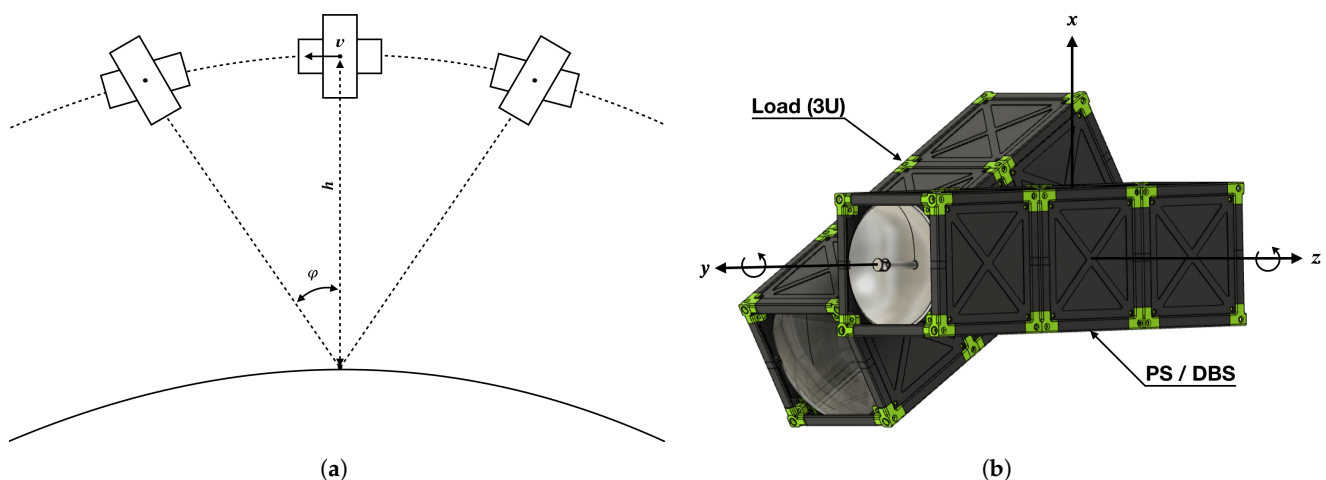


Figure 1. LEO operating conditions and 1 DoF pointing system. (a) Operation of the satellite with respect to the orbital configuration; (b) artistic illustration of a possible design of the satellite, which highlights the main components of the system.

2. Methodology

CubeSat-type satellites are mainly used for low cost and short duration scientific missions. The low overall cost, primarily linked to the small size of the satellites themselves, is also given by the positioning of the experiment in a *low Earth orbit* (LEO), which defines the main operating conditions.

The design criteria and the dynamics of the PS and DBS systems are now presented.

2.1. Pointing System

The typical operating conditions of LEO orbits, summarized in Table 1, allow us to give an estimate of the maximum angular velocity required to the *pointing system* (PS).

When tracking a ground object during a LEO trajectory, as depicted in Figure 1a, $\dot{\phi}$ varies from a maximum value of $\dot{\phi}_{max} = 0.0390$ rad/s, relative to an orbital height $h = 200$ km at the lower end of a LEO orbit [33], to a minimum value of $\dot{\phi} = 0.0130$ rad/s, relative to an orbital height $h = 600$ km. Much higher values can be reached when tracking other objects in space, i.e., other satellites. Given the maximum load angular velocity, and assuming the nominal speed of an electric motor acting on the pointing system $\dot{\phi}_e = 500 \text{ min}^{-1} = 52.35$ rad/s, it is now possible to calculate the needed value of the reduction ratio as $\tau_p = \dot{\phi}_r / \dot{\phi}_e = 1344$.

Table 1. Typical operating conditions of a low Earth orbit (LEO).

Parameter	Value
Altitude (h)	400–600 km
Velocity (v)	7.87–8.10 km/s
Revolution time	90 min
Temperature	−150/+200 °C

2.2. Dynamic Balancing System

The system is composed of three rigid bodies rotating of purely rotary motion around a common axis as described in Figure 2. Therefore, the dynamics of the single rotating body is described by Euler’s dynamic equation for rotational motion [34].

$$I \frac{d\Omega}{dt} + \Omega \times I\Omega = C \tag{1}$$

where I is the inertia tensor of the body with respect to the *body’s fixed reference frame* and C is the vector of the applied torques acting on the body. Assuming that the body is rotating about the z axis, which also corresponds to the principal axis of inertia, we can make some statements about the tensor I . First, the terms $I_{xz} = I_{zx} = I_{yz} = I_{zy} = 0$; second, although I is to be considered time-varying with respect to a fixed coordinate system, I is instead constant in time if referred to a local coordinate system. Therefore, the inertia tensor takes the following form:

$$I = \begin{bmatrix} I_{xx} & -I_{xy} & 0 \\ -I_{yx} & I_{yy} & 0 \\ 0 & 0 & I_{zz} \end{bmatrix} \tag{2}$$

The correct functioning of the PS, coupled with the DBS, must guarantee the precise positioning of the load while keeping the attitude of the CubeSat structure unchanged. Therefore, the rotational velocity vector of the body must have the following form:

$$\Omega = [\omega_x \quad \omega_y \quad \omega_z]^T \tag{3}$$

where $\omega_x = \omega_y = 0$. Replacing Equations (2) and (3) in Equation (1), the equation of motion of each rigid body rotating about the z axis is given by the following:

$$I_{zz}\dot{\omega}_z = C_z \tag{4}$$

Equation (4) refers to a single rigid body; therefore, in order to describe our system we introduce the following system of *ordinary differential equations* (ODEs) of the second order:

$$\begin{cases} I_{load_{zz}} \ddot{\phi}_p = C_1 \\ I_{cfw_{zz}} \ddot{\phi}_{cfw} = C_2 \\ I_{struct_{zz}} \ddot{\theta} = C_2 - C_1 \end{cases}, \tag{5}$$

where $I_{load_{zz}}$, $I_{cfw_{zz}}$ and $I_{struct_{zz}}$ are the inertia components along the z axis of the load, counter-rotating flywheel and structure bodies, respectively, while C_1 and C_2 are the

torques acting between the bodies. Finally, φ_p , φ_{cfw} , and ϑ are the coordinates which describe, respectively, their rotation, referring to a fixed coordinate system. In order to compute the system of equations in Equation (5), it is necessary to indicate the relationships that link the velocities given therein.

$$\varphi_p = \varphi + \vartheta \tag{6}$$

$$\varphi_{cfw} = \tau\varphi + \vartheta \tag{7}$$

where φ represents the rotation of the load with respect to a reference system solidal to the CubeSat structure containing the PS and DBS, and ϑ represents the rotation of the same CubeSat structure with respect to a reference frame fixed in space. Instead, τ is the unknown reduction ratio that binds the CFW and the load velocities. By deriving twice Equation (7) with respect to time, we obtain the relationships that link the accelerations of the three rigid bodies composing the system. Replacing the accelerations into Equation (5) and imposing the equilibrium condition of the CubeSat structure, i.e., $\alpha = [\ddot{\vartheta}_x \ \ddot{\vartheta}_y \ \ddot{\vartheta}_z] = [0 \ 0 \ 0]$, we obtain the following:

$$\begin{cases} I_{load_{zz}} \ddot{\varphi} = C_1 \\ I_{cfw_{zz}} \tau \ddot{\varphi} = C_2 \\ I_{struct_{zz}} \ddot{\vartheta} = C_2 - C_1 \end{cases} \tag{8}$$

This means that the condition of dynamic balancing along the z-axis $\ddot{\vartheta} = 0$ implies that the component of the torque acting on the structure is equal to the torque acting on the load; therefore, $C_2 = C_1$. A relationship is created between the first two equations in Equation (8), obtaining the following:

$$\begin{cases} I_{load_{zz}} \ddot{\varphi} = C_1 \\ (I_{cfw_{zz}} \tau - I_{load_{zz}}) \ddot{\varphi} = 0 \\ C_2 = C_1 \end{cases} \tag{9}$$

Therefore, the system of rigid bodies is balanced when $(I_{cfw_{zz}} \tau - I_{load_{zz}}) \ddot{\varphi} = 0$. This condition is obtained whether $\ddot{\varphi} = 0$ or the following holds:

$$\tau = \frac{I_{load_{zz}}}{I_{cfw_{zz}}} \tag{10}$$

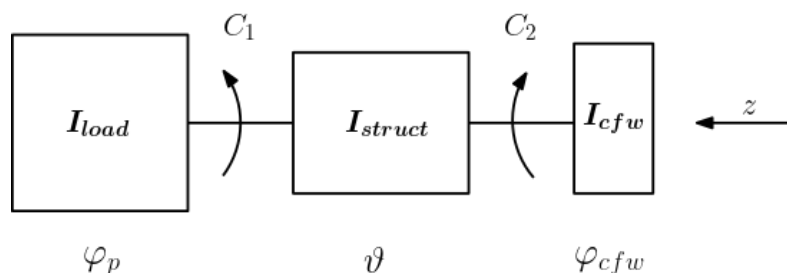


Figure 2. Diagram showing the main bodies composing the entire satellite and the torques exchanged between them.

2.3. Mechanical Reduction System

The τ values, calculated in Sections 2.1 and 2.2, suggest the necessity to design a high-density reduction ratio, given also the reduced internal volume available. The main mechanical reduction systems taken into consideration are the following:

- *Spur gear transmissions.*
- *Planetary gear transmissions.*
- *Compound planetary gear transmissions.*

Compared to spur-gear reduction systems, planetary gear systems offer, in a more compact volume, the same reduction ratios per stage. Still, in order to obtain the values shown in Section 2.1, a certain number of reduction stages connected in series are required. Therefore, compound planetary gear transmission is the selected system for this project.

The composite planetary gearboxes are characterized by the same basic elements of the planetary gear transmission. However, the way of coupling the various parts makes these systems much more performing in terms of τ_p while maintaining unchanged the occupied volume. The four configurations found in Ref. [35] are called Types A, B, C, D. Type A was chosen since, with the same reduction ratio, it has the fewest moving parts.

Moreover, the first stage planet gears and the second stage planet gears are directly connected, thus rotating at the same speed. The first stage ring gear is fixed, while the second stage ring gear is free to rotate, representing the output of the reduction system as shown in Figure 3a. In order to calculate the gear setup of C-PGT, the minimum number of teeth $z_{min} = z_1$ can be evaluated as follows:

$$z_{min} = \frac{2}{\sqrt{\tau_p^2 + (1 + 2\tau_p) \sin^2 \alpha + \tau_p}} \tag{11}$$

Imposing $\tau_p = 10$, representing the maximum reduction ratio per stage, and $\alpha = 25^\circ$, the angle of pressure of the gear, $z_{min} = 12$ is obtained. C-PGTs systems are based on planetary gears systems, and hence, two main design conditions must be met:

- Condition 1:

$$\phi_{RG} = \phi_{SG} + 2 \phi_{PG}$$

- Condition 2:

$$n = \frac{z_{SG} + z_{RG}}{n_{PG}}$$

where $n \in \mathbb{N}$, ϕ stands for the diameter of the gears, z for the number of teeth and n for the number of gears. The expression describing the reduction ratio, obtainable once values are assigned to the variables, is reported as follows:

$$\tau_p = \frac{1 + \frac{z_3}{z_1}}{\frac{1 - z_3}{(z_3 - z_1) z_6} (2z_6 - z_1 - z_3)} \tag{12}$$

By imposing $x = z_1/z_3$ and $y = z_6/z_3$, Equation (12) can therefore be simplified in the following:

$$\tau_p = \frac{1 + \frac{1}{x}}{\frac{1 - (2y - x - 1)}{y(1 - x)}} \tag{13}$$

Figure 3b shows how τ_p is strictly dependent from y ; in fact, as y approaches one, τ_p rapidly increases.

Therefore, the most efficient way to increase τ_p is to have z_6 and z_3 differing by one tooth. Considering the volume constraints and in compliance with the two previously reported design conditions, the reduction system setup is shown in Table 2.

Table 2. C-PGT gear setup and values of $I_{cfw_{zz}}$ for all payload configurations.

Gear Setup	Load	$I_{cfw_{zz}}$ [kg · m ⁻²]
$z_1 = 12$	1u	-7.40×10^{-7}
$z_2 = 36$	2u	5.06×10^{-6}
$z_3 = 84$	3u	1.95×10^{-5}
$z_5 = 35$	4u	4.71×10^{-5}
$z_6 = 83$	5u	9.20×10^{-5}

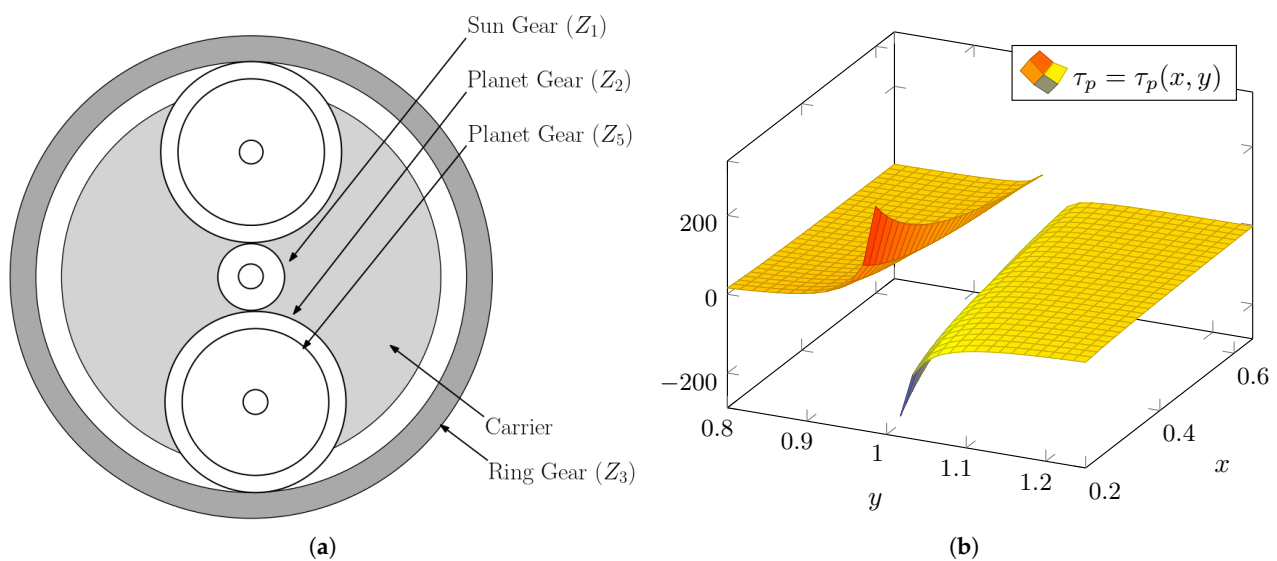


Figure 3. Compound planetary gear transmission (C-PGT) basic components: Type A configuration. (a) General diagram of the system; the transmission output is the ring gear Z_6 , not shown in the figure, that meshes with two planet gears Z_5 . (b) The y and x dependence, shown to the reduction ratio τ_p .

By combining the values shown in Table 2 into Equation (12), a reduction ratio of $\tau_p = 498$ is obtained. This value is not sufficient, compared to the requirements reported in Sections 2.1 and 2.2. Therefore, a $\tau = -3$ PGT is installed as input to C-PGTs, obtaining a total reduction ratio of $\tau_p = \tau(498) = -1494$. The minus sign suggests that the input gear rotates in an opposite direction with respect to the output ring. This condition is necessary in order to balance the total angular momentum of the system. The CFW inertia is defined by combining the load inertia values seen in Table 2 for all configurations, with the aforementioned DB condition indicated in Section 2.2.

2.4. Material Selection

The *fused filament fabrication* (FFF) represents the most economical and perhaps dif-fused 3D printing technique, allowing the creation of pieces of excellent quality and high mechanical resistance. In order to establish a material's selection criteria, a description of the requirements relative to the operating environment is needed. During each revolution around Earth, satellites are immersed in a thermal field which varies between 200 °C and -160 °C [13]. At an altitude of 200 km, the atmospheric density is $\rho = 10 \times 10^{-10} \text{ kg} \cdot \text{m}^{-3}$, while the pressure varies between $P_{in} = 1.33 \times 10^{-9} \text{ mbar}$ and $P_{out} = 1.33 \times 10^{-6} \text{ mbar}$ on the outside and on the inside of the satellite, respectively. These high vacuum conditions cause *outgassing*; additionally, for the same reason, the use of greases and oil for lubrication must be avoided.

Four main material characteristics, along with their constraint value, compose the selection criteria needed to determine the most suitable printing material for our intent: low static and dynamic friction coefficients ($\mu < 0.25$), resistance to *outgassing* (TML < 1%), high mechanical strength ($R_m > 50$) and a wide range of thermal resistance *CUT*. In Table 3, all printing materials suited for FFF are listed along with their main characteristics. Given the wide range of choice, two different group materials are selected: one for the CubeSat structure, and one for the C-PGT.

Considering the selection criterion parameters, the optimal printable materials are reported in Table 4 along with their main technical characteristics.

Table 3. FFF printing materials characteristics.

Material	R_m [MPa]	CUT [°C]	TML [%]	μ	PT [°C]	[kg]
ABS	25–40	65–100	0.17	0.08–0.46	250	10–40
PLA	65	52	0.56	0.38–0.5	220	10–40
PA	48–85	100–150	1.09–12.43	0.15–0.25	270	25–65
PETG	53	80–140	0.35	0.22	250	20–60
POM	77	80–105	0.47	0.2	260	20–50
PC	72	100–140	0.17	0.38–0.5	310	40–75
PEEK	105	154–260	0.27	0.51	410	600
PEI	64	170–200	0.07	0.45	390	180–210

Table 4. Main characteristics of the printing materials.

Properties	ANTERO 800NA	ULTEM™ 1010	3DXSTAT™	POM-C (AH SD)	iglidur® J260-PF
ρ [kg·m ⁻³]	1280	1270	1280	1350	1350
CUT [°C]	150	216	−40/+80	−60/+100	−100/+120
α [μm m ⁻¹ °C ⁻¹]	39–53	41–47	41–47	17	13
R_m [MPa]	90.6	81	50	40	43
R_{02} [MPa]	90.6	64	50	40	43
R_f [MPa]	140	144	74	46	46
TML [%]	0.27	0.58	-	-	-
ϵ [%]	-	-	23	23	13

The CubeSat structure must endure the toughest conditions; because of this, the selected materials are PEEK and PEI, indicated by their commercial names ANTERO and ULTEM, respectively. Instead, the PS is positioned inside the CubeSat structure together with the control boards, the inertia disk and the electric motor. Being shielded from direct sun radiation exposure translates into a narrower temperature range, compared to external conditions. Normally, gearboxes are lubricated by means of specific oils or greases in order to reduce friction and wear between the parts and to dissipate heat. However, common lubricants cannot be used in space, due to susceptibility to low-pressure evaporation. As such, low-friction materials ($\mu < 0.3$) with good values of $R_m > 50$ MPa are promising candidates; PA, PETG and POM are identified as the best amongst those considered in this study: iglidur®, 3DXSTAT™ and POM-C, respectively.

Having already fixed the gears characteristics, setting the *polylactic acid* (PLA) as the prototype printing material and considering also the maximum mechanical stresses present in the C-PGT, we proceeded in accordance with the theory concerning 3D-printed spur gears [23,24,36], imposing an optimal thickness ($b = 5$ mm) common to all gears, useful to provide a certain safety margin. The reduction system was then modeled using Fusion 360® software, paying attention to the constraints given by the containment structure.

2.5. Motor Control System

Actuators in space are usually classified as active and passive. Passive systems are those operated by spring mechanisms, i.e., deployment systems, while active systems are those operated by electric motors and related control electronics [32,37,38]. The selection of the motor was based on considerations regarding the high-vacuum environment found in orbit [39]. Taking *brushed* motors, *stepper* motors and *brushless* motors (BLDC) into consideration, the optimal choice for our purpose fell on BLDC motors. The choice was justified by the greater reliability and excellent ratio between the weight and torque generated. In order to set up and test the prototype, a simple open loop speed control is designed. An electronic speed control (ESC), composed by three TIP122G transistors, three 1N5817 schottky diodes and three 1k resistors is assembled. The control software is composed of a loop cycle that controls the motor phases excitation time, starting from a maximum value

of $\delta_{max} = 80$ ms to $\delta_{min} = 20$ ms in a period of 15 s. Once δ_{min} is reached, the activation time profile is kept constant. In order to convert the time steps in the rotational speed of the payload, the following equation is used:

$$\dot{\phi}_{load} = \frac{2 \pi}{0.001 p \delta \tau_p} \quad (14)$$

where the only unknown parameter is $p = 12$, representing the number of motor poles.

3. Numerical Analysis and Experimental Campaign

Wanting to test the results obtained so far, a prototype of the PS-DBS is realized and tested. The experimental results are then compared with the analytical model presented in Section 2.2, realized in MATLAB, and with the multi-body simulation realized by means of the ADAMS environment.

3.1. Multi-Body Simulation

In order to prove the soundness and the effectiveness of the proposed mechanism, a simulation using the commercial software MSC ADAMS is performed. In particular, the motor reduction and the first and the second stages of the C-PGTs gear box are modeled by using the machinery ADAMS toolbox. Hence, the rest of the model, such as the rod, the inertia ring and the structure, is constructed around the gearbox. These are modeled with ideal bodies to which inertial properties are applied coherently with the experimental setup. Appropriate kinematic joints link the separate components. The final model can be seen in Figure 4a.

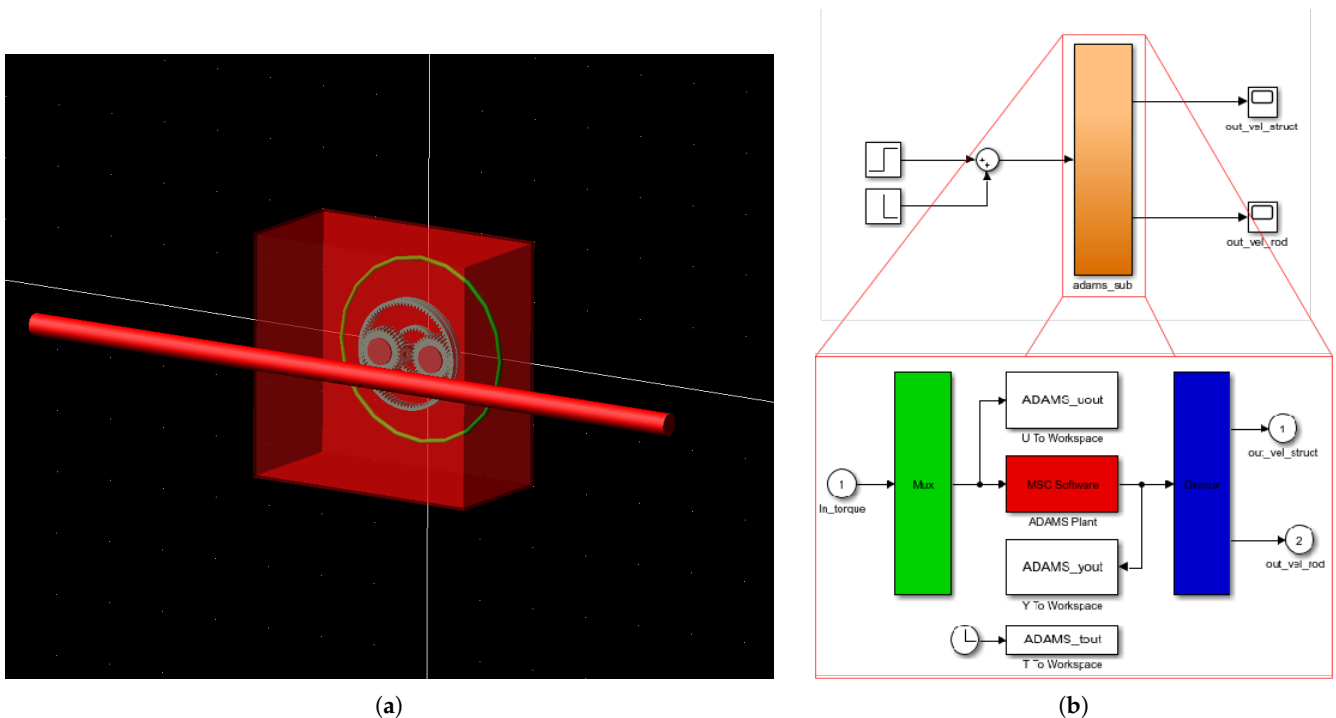


Figure 4. ADAMS/SIMULINK co-simulation setup. (a) 3D view of the CubeSat unit modeled in ADAMS; (b) ADAMS/SIMULINK co-simulation plant layout.

The micro-gravity simulation environment is subject to a single external force, i.e., the torque exerted by the ideal DC motor, acting between the structure and the inertia rings. The simulations are conducted in the context of the ADAMS/SIMULINK co-simulation. The modeled torque is the controllable variable that is exported as an input state variable for the ADAMS/SIMULINK co-simulation. For what concerns the output state variables, these are the angular velocity of the rod and the structure. Finally, in order to enable the

multi-body simulation, the ADAMS plant is exported, and simulations are conducted through Simulink. In particular, the Simulink model setup can be seen in Figure 4b.

In this context, the torque is modeled as a pulse having an amplitude and width equal to $C(\theta)$ and 15 s, respectively, which ensure a trapezoidal speed profile and represent the one used for the experimental campaign. Simulations are conducted for both the cases of *balanced* and *unbalanced* pointing system.

3.2. Prototype and Experimental Setup

The mechanical reduction system setup and the selected materials information are translated into digital CAD file, as shown in Figure 5a,b. Once completed, the system is printed, as shown in Figure 5c, using a Creality Ender 3 FFF printer, selecting a list of printing parameters granting a middle ground between print time and mechanical strength (see Table 5).

Table 5. Prototype printing parameters.

Parameters	Value
Material	PLA
Layer height	0.2 mm
Infill percentage	30%
Infill geometry	Gyroid
Wall thickness	0.4 mm
Print speed	60 mm/s
Nozzle temp.	200 °C
Bed temp.	60 °C

The overall printing process takes 14 h 34 min to print 21 pieces by fusing 47.78 m of PLA filament, corresponding to 135 g of material.

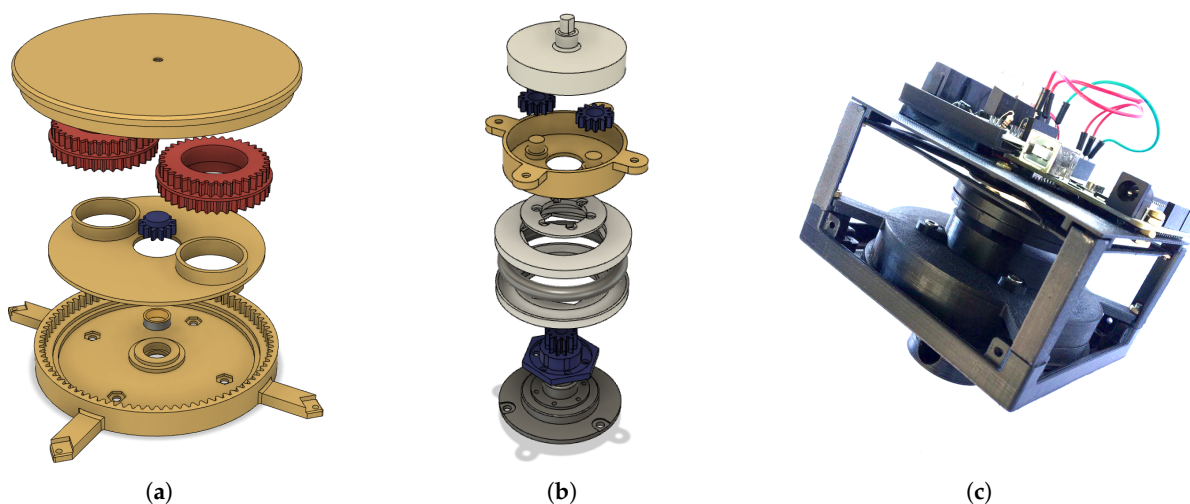


Figure 5. Design of the prototype. (a) An exploded view of the C-PGTs gearbox. (b) An exploded view of the first primary reduction gear together with the motor and flywheel. (c) The 3D-printed prototype, which is installed in a 1/2 CubeSat unit.

The toroidal-shaped CFW implemented in the prototype has a slightly different inertia $I_{cfw_{zz}}$ (see Table 6), compared to that calculated in Table 2 for a 3u payload. Therefore, a testing payload is calculated and realized by means of a threaded rod and two weights mounted on a threaded support.

Table 6. CFW and test payload masses and inertia.

Component	Material	Mass [g]	I_{zz} [$\text{kg}\cdot\text{m}^2$]
CFW	Steel	31.72	0.00002232
Rod	Steel	376.08	0.0116
Weight	Steel	72.00	0.0086

In order to test the prototype, a micro gravity-like environment is recreated to simulate orbital conditions. The prototype is hung to the laboratory ceiling via a Nylon cable with length $L = 2$ m and diameter $\phi = 0.5$ mm, as shown in Figure 6. The experiment lasts 30 s during which 900 frames are extracted and processed by means of the MATLAB image processing toolbox. In order to verify the PS effectiveness, with Figure 6a as reference, the absolute payload angular position $\varphi(t) = \varphi_r(t) + \vartheta(t)$ is recorded, and in order to verify the DBS effectiveness, the angular displacement $\vartheta(t)$ of the CubeSat structure with respect to the fixed reference frame $O_{x,y}$ is recorded, testing the system once with full load inertia $I_{load} = 0.0320$ $\text{kg}\cdot\text{m}^2$ and once with reduced load inertia $I_{load} = 0.0116$ $\text{kg}\cdot\text{m}^2$, i.e., without weights.

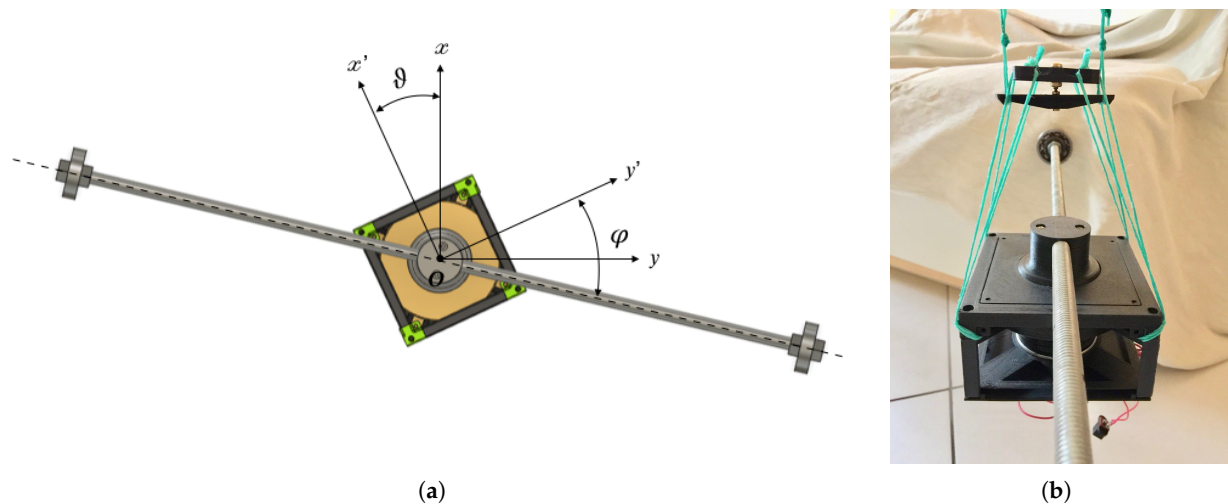


Figure 6. Experimental setup. (a) Top view of the system; the $O_{x',y'}$ reference frame is fixed to the CubeSat structure, while $O_{x,y}$ is fixed to the ground. The letter ϑ indicates the rotation around the $z = z'$ axis between $O_{x',y'}$ and $O_{x,y}$, while φ_r indicates the payload angular position with respect to $O_{x',y'}$. (b) The prototype mounted on the low-friction joint ready for the experimental campaign.

4. Results and Discussion

The PS experimental test results, along with the data obtained by the multi-body and analytical models are shown in Figures 7a and 8a, and in Table 7. The plots in Figure 7a compare the functions $\varphi(t)$ obtained from the analytical model and those from the multi-body simulation, with the experimental data extracted from the videos of the experimental campaign, captured using the *image processing toolbox*. The highest load displacement values, corresponding to $\varphi(t = 30)$ are reported in Table 7. The analytical model reaches the maximum displacement of $\varphi = 25.31^\circ$. This shows a slightly different trend with respect to the experimental $\varphi = 24.42^\circ$ and the multi-body simulation that, instead, reaches a value of $\varphi = 24.87^\circ$. It is clear that between the two models, the one that mostly adheres to the experimental data is the multi-body. This result highlights the better capability of ADAMS in predicting the dynamic variables trend. In Figure 8a, the comparison between the experimental data for the balanced (B) and an unbalanced (U) PS is shown. The experimental absolute angular position for the unbalanced solution diverges rapidly with respect to the balanced case, reaching a value of angular displacement $\varphi_U = 116.80^\circ$,

almost 5 times higher than the nominal value of $\varphi_B = 24.42^\circ$. It is worth noting that a value so high is given by the small satellite payload inertia involved in the experimental test, compared to the sources of error (e.g., gearbox). In a real setup, such as that shown in Figure 1b, where the fixed side is composed of three aligned CubeSats units, we expect φ_U to be considerably narrower.

Another fundamental parameter which was considered in the experimental campaign is the payload angular velocity. The maximum relative angular velocity is $\dot{\varphi} = 0.0174$ rad/s, a value which is within the required speed range set in Section 2.1, and corresponds to the value imposed by means of Equation (14), thus proving the efficiency of the actuator and the accuracy of its open loop control system.

Table 7. Experimental data extrapolated from the video and values obtained from the analytical model and the multi-body simulation, for φ and ϑ both for balanced (B) and unbalanced (U) configurations.

Data	$\varphi_B [^\circ]$	$\varphi_U [^\circ]$	$\vartheta_B [^\circ]$	$\vartheta_U [^\circ]$
Analytical	25.31	-	0.0699	-
Multi-body	24.87	-	0.0725	-
Experimental	24.42	116.80	0.0745	3.24

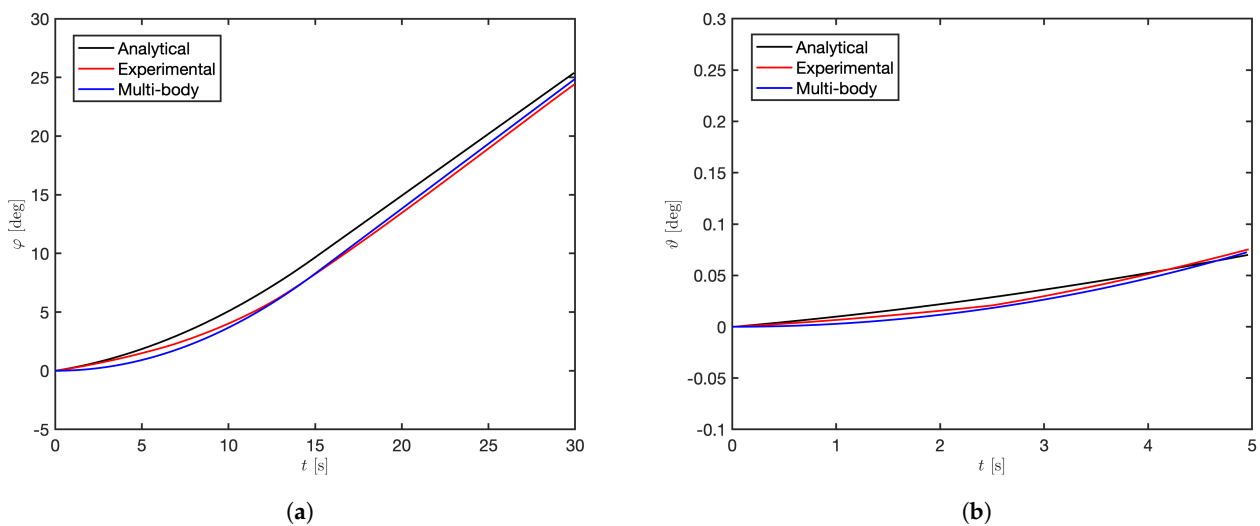


Figure 7. Experimental results validation. (a) Comparison between the experimental load absolute angular position (φ) and the analytical and multi-body models; (b) the comparison between the experimental structure angular position (ϑ) for the balanced solution, and the analytical and multi-body models.

The DBS experimental results are shown in Figures 7b and 8b, and in Table 7. Figure 7b compares $\vartheta(t)$, obtained in the experimental campaign with full load inertia, with the analytical and multi-body models. The model that most adheres to the experimental results for what concerns to the PS is that which is obtained with the multi-body simulation. In Figure 8b, we highlight the difference between the experimental results for the balanced $\vartheta(t)_B$ and unbalanced $\vartheta(t)_U$ solution. In the first 5 s of simulation, the dynamically balanced prototype reaches the maximum displacement of $\vartheta_B = 0.0745^\circ$, maintaining the structure attitude along the z axis, being fairly unchanged, while the unbalanced prototype reaches the maximum displacement of $\vartheta_U = 3.24^\circ$. These results show the vital importance of a correctly designed DBS; the two experimental results, in fact, differ by two orders of magnitude. The results obtained for the balanced solution prove also the correctness of the mechanical reduction system design.

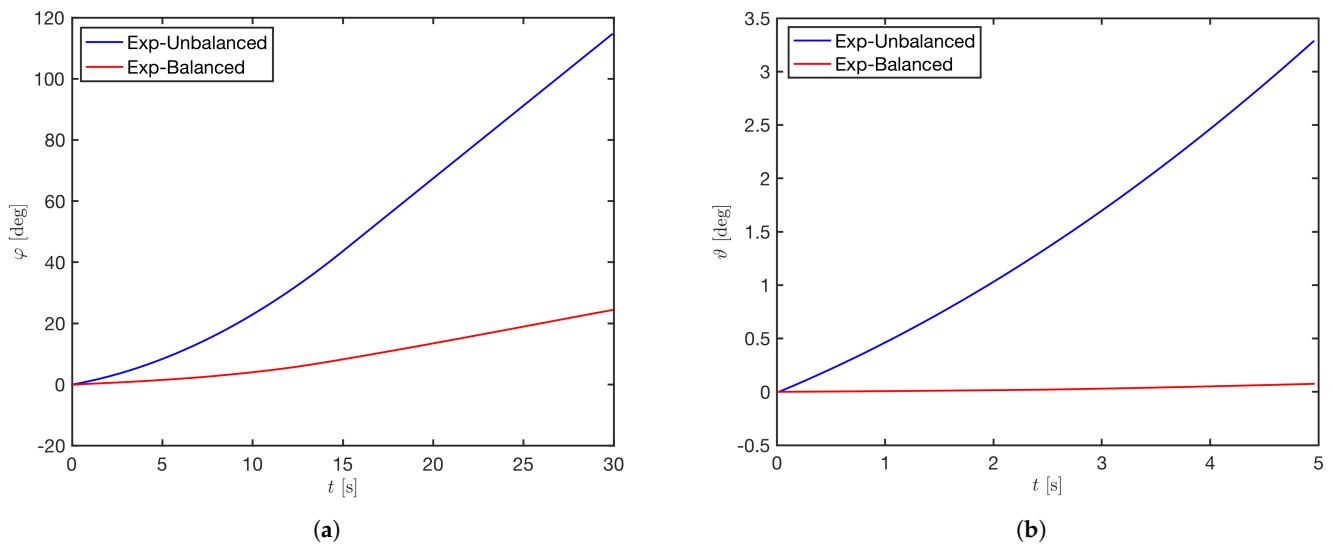


Figure 8. Experimental results validation. (a) Comparison between the experimental load absolute angular position (φ) for the unbalanced (Exp-Unbalanced) and balanced solutions (Exp-Balanced); (b) comparison between the experimental structure angular position (θ) for the unbalanced (Exp-Unbalanced) and balanced solutions (Exp-Balanced) is shown.

Moreover, the experimental results show a remarkable adherence of the analytical and numerical models with the experimental results. The small differences can be ascribable to many factors, such as friction, poor clearance between moving 3D-printed parts, or the approximations used in the definition of the inertia parameters.

The experimental campaign has, therefore, successfully verified the correct functioning of the proposed PS. The system is suitable for rotating at least a 3U CubeSat, within the speed range established in Section 2.2. In addition, the FFF printing technique has produced a prototype with accurate precision, especially for what concerns the parts present within the reduction system, being able to withstand the mechanical stresses generated during the test, even with a low-performance material such as PLA.

Furthermore, during the experiments, the effectiveness of the DBS was proven; in its absence, the correct positioning of the load would be impossible without ACS to compensate. In fact, it is seen how the presence of the CFW, combined with a high-density reduction system, such as the C-PGTs, allows to greatly reduce the rotations of the overall structure, leaving only the small final corrections to the ACS.

5. Conclusions

In this work, we tested a different designing and manufacturing approach to the realization of a vital component of CubeSat satellites: the pointing system (PS). The PS is capable of rotating a payload composed by a certain number of CubeSat units, and was designed and tested along with an integrated dynamic balancing system, both operated by the same brushless DC motor. The choice of incorporating a dynamic balancing system (DBS) directly in the PS avoids the necessity to have a dedicated electronic control board for the dynamic balance of the satellite. However, we are aware that an attitude control system is still useful for small attitude corrections. Going further, adapting to the Cubesat satellite philosophy and focusing on the economy of bulk space and weights, we have designed the whole system in order to be 3D printed and installed inside a half-unit module. To this end, we paid particular attention to the type of infill pattern to be used for the realization of our prototype. In fact, it is well known that by using an infill pattern, it is possible to achieve the same or even better mechanical properties than a solid printed piece, with a consequent saving of material and therefore of weight [40]. Among the various types of pattern available, we preferred the “Gyroid” type because in addition to having significant

vibration absorption properties, it is 23.7% faster and up to 12.59% more resistant in terms of tensile strength, compared to a “honeycomb” infill type [41].

In Section 2.4, the research of AM compatible materials suitable for the difficult operational conditions of the LEO orbits allowed us to determine the best candidates, such as PEEK and PEI for the CubeSat structure, where the thermal and mechanical stresses dictate the material characteristic requests. On the other hand, POM, PETG and Igildur were identified as candidates for the PS mechanical reduction system, where, in addition to the aforementioned requirements, the auto lubrication of the moving parts is needed. However, our materials research did not consider issues related to the effects of gamma rays. The materials selected by us, suitable to withstand thermal conditions, outgassing and mechanical stress, must be specially coated so as not to degrade, due to the rays themselves. In order to verify the design, a PLA prototype was fabricated and tested along with its actuation system. This proved the correct functioning of the PS and DBS design, and the advantage of additive manufacturing, such as good dimensional accuracy and reduced weight of the components (the 1/2 u CubeSat along with the PS and DBS weighs no more than 0.3 kg, comprehensive of the electronic board and BLDC motor).

Given the results obtained on the prototype, we believe that AM is suited for the creation of satellite parts as complex as the reduction system designed in this work. In addition, the possibility of producing components directly in orbit—for example, on the ISS—would allow the rapid creation and modification of parts without having to wait for supplies from the ground. Moreover, we can avoid subjecting the most delicate parts to mechanical stress due to the launch. In fact, the realization via AM of a functioning CubeSat directly on ISS, printed and assembled by astronauts, is not a novelty as demonstrated in the MakerSat-1 mission [42].

Author Contributions: Conceptualization, N.S.G.; methodology, N.S.G. and M.C.; software, N.S.G. and M.C.; validation, N.S.G. and M.C.; formal analysis, N.S.G. and M.C.; investigation, N.S.G. and M.C.; resources, N.S.G. and M.C.; data curation, N.S.G. and M.C.; writing—original draft preparation, N.S.G., M.C., P.G. and S.S.; writing—review and editing, N.S.G., M.C., P.G. and S.S.; visualization, N.S.G. and M.C.; supervision, P.G. and S.S.; project administration, P.G. and S.S.; funding acquisition, P.G. and S.S. All authors have read and agreed to the published version of the manuscript.

Funding: The work presented in this paper was developed with funding from the University of Trieste via the project “University funding for scientific Research projects—FRA 2018”, from the Italian Space Agency through the “ACCORDO ATTUATIVO n. 2020-27-HH.0 nell’ambito dell’ACCORDO QUADROASI-UNIVERSITA’ DEGLI STUDI DI TRIESTE n. 2019-7-Q.0” and from the PRIN project SEDUCE” n. 2017TWRCNB.

Institutional Review Board Statement: Not applicable.

Informed Consent Statement: Not applicable.

Data Availability Statement: The data presented in this study are available upon reasonable request from the corresponding author.

Conflicts of Interest: The authors declare no conflict of interest. The funders had no role in the design of the study; in the collection, analyses, or interpretation of data; in the writing of the manuscript, or in the decision to publish the results.

References

1. Antunes, S. *Surviving Orbit the DIY Way*; O’Reilly Media, Inc.: Sebastopol, CA, USA, 2012.
2. Villela, T.; Costa, C.; Brandão, A.; Bueno, F.; Leonardi, R. Towards the Thousandth CubeSat: A Statistical Overview. *Int. J. Aerosp. Eng.* **2019**, *2019*, 1–13. [CrossRef]
3. Waydo, S.; Henry, D.; Campbell, M. CubeSat design for LEO-based Earth science missions. In Proceedings of the IEEE Aerospace Conference Proceedings, Big Sky, MT, USA, 9–16 March 2002; Volume 1.
4. Sweeting, M.N. Modern Small Satellites-Changing the Economics of Space. *Proc. IEEE* **2018**, *106*, 343–361. [CrossRef]
5. The CubeSat Program. CubeSat Design Specification Rev. 13. California Polytechnic State University. 2014. Available online: http://www.cubesat.org/s/cds_rev13_final2.pdf (accessed on 23 August 2021).

6. Becedas, J.; Caparrós, A. *Additive Manufacturing Applied to the Design of Small Satellite Structure for Space Debris Reduction*; IntechOpen Limited: London, UK, 2018; Volume 1.
7. Stevenson, T.H.; Lightsey, E.G. Design and optimization of a multifunctional 3D-Printed structure for an inspector Cubesat. *Acta Astronaut.* **2020**, *170*, 331–341. [[CrossRef](#)]
8. Ricco, A.J.; Maria, S.R.S.; Hanel, R.P.; Bhattacharya, S. BioSentinel: A 6U Nanosatellite for Deep-Space Biological Science. *IEEE Aerosp. Electron. Syst. Mag.* **2020**, *35*, 6–18. [[CrossRef](#)]
9. Piattoni, J.; Candini, G.P.; Pezzi, G.; Santoni, F.; Piergentili, F. Plastic Cubesat: An innovative and low-cost way to perform applied space research and hands-on education. *Acta Astronaut.* **2012**, *81*, 419–429. [[CrossRef](#)]
10. Marshall, W.M.; Stegeman, J.D.; Zemba, M.; MacDonald, E.; Shemelya, C.; Wicker, R.; Kwas, A.; Kief, C. Using Additive Manufacturing to Print a CubeSat Propulsion System. In Proceedings of the 51st AIAA/SAE/ASEE Joint Propulsion Conference, Orlando, FL, USA, 27–29 July 2015.
11. Corpino, S.; Caldera, M.; Nichele, F.; Masoero, M.; Viola, N. Thermal design and analysis of a nanosatellite in low earth orbit. *Acta Astronaut.* **2015**, *115*, 247–261. [[CrossRef](#)]
12. Kang, S.J.; Oh, H.U. On-Orbit Thermal Design and Validation of 1 U Standardized CubeSat of STEP Cube Lab. *Int. J. Aerosp. Eng.* **2016**, *2016*, 4213189. [[CrossRef](#)]
13. Gorev, V.; Pelemeshko, A.; Zadorozhny, A.M.; Sidorchuk, A. Thermal deformation of 3U CubeSat in low Earth orbit. *MATEC Web Conf.* **2018**, *158*, 01013. [[CrossRef](#)]
14. Anwar, A.; Elfiky, D.; Hassan, G.; Albano, M.; Marchetti, M. Outgassing Effect on Spacecraft Structure Materials. *Int. J. Astron. Astrophys. Space Sci.* **2015**, *2*, 34–38.
15. Zwicker, A.; Bloom, J.; Albertson, R.; Gershman, S. The suitability of 3D printed plastic parts for laboratory use. *Am. J. Phys.* **2015**, *83*, 281–285. [[CrossRef](#)]
16. Povilus, A.; Wurden, C.; Vendeiro, Z.; Baquero-Ruiz, M.; Fajans, J. Vacuum Compatibility of 3D-Printed Materials. *J. Vac. Sci. Technol. A Vac. Surf. Films* **2013**, *32*, 033001. [[CrossRef](#)]
17. Jiao, Z.; Jiang, L.; Sun, J.; Huang, J.; Zhu, Y. Outgassing Environment of Spacecraft: An Overview. *IOP Conf. Ser. Mater. Sci. Eng.* **2019**, *611*, 012071. [[CrossRef](#)]
18. Murcia Piñeros, J.O.; dos Santos, W.A.; Prado, A.F. Analysis of the orbit lifetime of CubeSats in low Earth orbits including periodic variation in drag due to attitude motion. *Adv. Space Res.* **2020**, *67*, 902–918. [[CrossRef](#)]
19. Slejko, E.; Gregorio, A.; Lughi, V. Material Selection for a CubeSat Structural Bus Complying with Debris Mitigation. *Adv. Space Res.* **2020**, *67*, 1468–1476. [[CrossRef](#)]
20. Cappelletti, C.; Battistini, S.; Malphrus, B. *The CubeSat Handbook: From Mission Design to Operations*; Elsevier: Amsterdam, The Netherlands, 2020; p. 498.
21. Costa, J.R.; Lima, E.B.; Fernandes, C.A. Compact Beam-Steerable Lens Antenna for 60-GHz Wireless Communications. *IEEE Trans. Antennas Propag.* **2009**, *57*, 2926–2933. [[CrossRef](#)]
22. Bekkar Djelloul Saiah, S.; Bensikaddour, E.; Kaddouri, A.; Belbachir, R.; Nasri, B.; Baba Hamed, D.E. Analysis of the communication links between the AlSat-1b satellite and the ground station: The impact of the Auto Tracking system on antenna pointing accuracy. *Int. J. Satell. Commun. Netw.* **2021**, *39*, 486–499. [[CrossRef](#)]
23. Dimić, A.; Miskovic, Z.; Mitrovic, R.; Ristivojević, M.; Zoran, S.; Danko, J.; Bucha, J.; Milesich, T. The Influence of Material on the Operational Characteristics of Spur Gears Manufactured by the 3D Printing Technology. *J. Mech. Eng.* **2018**, *68*, 261–270. [[CrossRef](#)]
24. Zhang, Y.; Mao, K.; Leigh, S.; Shah, A.; Chao, Z.; Ma, G. A parametric study of 3D printed polymer gears. *Int. J. Adv. Manuf. Technol.* **2020**, *107*, 1–12. [[CrossRef](#)]
25. Kalavadiya, R.; Kalal, S.; Dodia, D.; Zaveri, P. *Optimization of Infill Patterns for Spur Gear in 3D Printing Using PLA*; Gardi College of Engineering and Technology: Rajkot, India, 2017.
26. Dobariya, M. Design of Compound Planetary Gear Train. *Int. J. Res. Appl. Sci. Eng. Technol.* **2018**, *6*, 3179–3184. [[CrossRef](#)]
27. Arnaudov, K.; Karaivanov, D. Higher compound planetary gear trains. *VDI Berichte* **2005**, *1904*, 327–344.
28. Samanuhut, P.; Dogan, A. Dynamics Equations of Planetary Gear Sets for Shift Quality by Lagrange Method. In Proceedings of the Dynamic Systems and Control Conference, Ann Arbor, MI, USA, 20–22 October 2008; pp. 353–360.
29. Zhao, T. Modeling and Optimal Shift Control of a Planetary Two-Speed Transmission. *World Electr. Veh. J.* **2019**, *10*, 53. [[CrossRef](#)]
30. Zhang, H.; Zhao, X.; Yang, J.; Zhang, W. Optimizing Automatic Transmission Double-Transition Shift Process Based on Multi-Objective Genetic Algorithm. *Appl. Sci.* **2020**, *10*, 7794. [[CrossRef](#)]
31. Zhao, X.; Li, Z. Data-Driven Predictive Control Applied to Gear Shifting for Heavy-Duty Vehicles. *Energies* **2018**, *11*, 2139. [[CrossRef](#)]
32. Celikel, R.; Ozdemir, M.; Aydogmus, O. Implementation of a flywheel energy storage system for space applications. *Turk. J. Electr. Eng. Comput. Sci.* **2017**, *25*, 1197–1210. [[CrossRef](#)]
33. Allen, C.S.; Giraudo, M.; Moratto, C.; Yamaguchi, N. Chapter 4—Spaceflight environment. In *Space Safety and Human Performance*; Sgobba, T., Kanki, B., Clervoy, J.F., Sandal, G.M., Eds.; Butterworth-Heinemann: Oxford, UK, 2018; pp. 87–138.
34. Sidorenko, V. *Rotational Dynamics*; Keldysh Institute: Moscow, Russia, 2014.

35. Crispel, S.; Lopez Garcia, P.; Verstraten, T.; Convens, B.; Saerens, E.; Vanderborght, B.; Lefeber, D. Introducing Compound Planetary Gears (C-PGTs): A Compact Way to Achieve High Gear Ratios for Wearable Robots. In Proceedings of the 4th International Symposium on Wearable Robotics, WeRob2018, Pisa, Italy, 16–20 October 2018; pp. 485–489.
36. Redwood, F.B.; Schoffer, B. *The 3D Print Handbook. Technology, Design and Applications*; 3D HUBS: Amsterdam, The Netherlands, 2017.
37. Caligaris, S.L.; Fava, C.T. *Manuale di Meccanica*; HOEPLI: Milano, Italy, 2016.
38. Bolzern, P.G.E.; Scattolini, R.; Schiavoni, N.L. *Fondamenti di Controlli Automatici*; McGraw-Hill: New York City, NY, USA, 2014.
39. Favre, E.; Wavre, N.; Gay-Crosier, P.; Verain, M. *European Electric Space Rated Motors Handbook*; European Space Mechanisms and Tribology Symposium: Toulouse, France, 1999.
40. Belarbi, Y.E.; Guessasma, S.; Belhabib, S.; Benmahiddine, F.; Hamami, A.E.A. Effect of Printing Parameters on Mechanical Behaviour of PLA-Flax Printed Structures by Fused Deposition Modelling. *Materials* **2021**, *14*, 5883. [[CrossRef](#)]
41. Joska, Z.; Andrés, L.; Dražan, T.; Manas, K.; Pokorný, Z.; Sedlak, J. Influence of the shape of the filling on the mechanical properties of samples made by 3D printing. *Manuf. Technol.* **2021**, *21*, 199–205.
42. Campbell, B.; Nogales, C.; Grim, B.; Kamstra, M.; Griffin, J.D.; Parke, S. On-Orbit Polymer Degradation Results from MakerSat-1: First Satellite Designed to Be Additively Manufactured in Space. In Proceedings of the 34th Annual Small Satellite Conference, Utah State University, Logan, UT, USA, 1–6 August 2020.